State-dependent Atom Transport in Polarization Synthesized Optical Lattices: An Estimation of Dephasing Influences

Bachelor Thesis

at the
Mathematisch-Naturwissenschaftlichen Fakultät
der

Rheinischen Friedrich-Wilhelms-Universität Bonn

Name:	Jana Sanne Huisman
First reviewer:	Prof. Dr. Dieter Meschede
Second reviewer:	Dr. Frank Vewinger

Bonn; August 2, 2013

Contents

1 Introduction

In 1982 Feynman first proposed the idea of a quantum simulator, based on the fact that only a quantum system can simulate other quantum systems in non-exponential runtimes [2]. Since then many different quantum experiments have been devised to allow for best control and easiest access to quantum mechanical observables. Ultracold atoms in optical lattices are successful simulators of quantum phenomena, that allow many degrees of freedom for experimentation [7].

A quantum computer, the quintessential quantum simulator, makes use of quantum bits (qubits) to manipulate and store quantum information. In the 1D Quantum Walk experiment the qubit is formed by the $|F = 4, m_F = 4\rangle$ and $|F = 3, m_F = 3\rangle$ hyperfine levels of the cesium ground state. To enable quantum simulations, the ultracold cesium atoms are trapped in a standing wave optical dipole trap, created by interference between two linearly polarized counter-propagating beams. In the 1D Quantum Walk experiment one dipole trap beam consists of a synthesized linear polarization made by two superimposed, circularly polarized beams, which allows spin-dependent, one dimensional atom transport.

The aim of this thesis was to quantify the decoherence mechanisms within the 1D Quantum Walk experiment. An important aspect of qubits is their ability to retain quantum information. A loss of such information, called decoherence, inevitably results from the interaction between the qubit and its environment. The characteristic timescale on which decoherence becomes important is called the coherence time, and it depends strongly on the realization of the qubit, and thus on the experimental setting. To quantify the decoherence mechanisms, I tried to create a structured overview of the decoherence mechanisms at play, and their origins within the polarization set-up of the experiment. I partly built on the knowledge of decoherence that has been amassed with previous versions of this experiment [11, 17, 18], combining the characterizations and extending them to the most current set-up. In addition I performed a series of measurements to improve the polarization purity of the set-up.

In chapter 2 I review the interaction between atom and light field, as well as the principle of state-dependent transport, which underlie the 1D Quantum Walk experiment. Subsequently I discuss a definition and typology of coherence times as well as the method used to measure this value in chapter 3. In general decoherence is influenced by fluctuations of experimental parameters from their ideal value. I describe the types of fluctuations and the characterization of decoherence mechanisms in chapter 4.

Since the experiment is subject to continuous updates and improvement, in chapter 5 the current experimental set-up is explained, and the influence of individual components upon the coherence time is studied to a greater extent. Here special emphasis is placed on a combining fiber, which currently seems to limit the polarization purity of the synthesized beam. Since this seems to be the limiting factor, I looked into alternatives for the current fiber, as described in section 5.3. In chapter 6 I summarize and conclude the thesis.

2 Principles of operation

In quantum optics the interaction between ultracold atoms and light fields plays a central role. The oscillating electromagnetic field $\vec{E}(\vec{r},t)$ induces a time-dependent dipole moment $\vec{d}(\vec{r},t)$ in the atom as a function of the wavelength and the intensity of the incident light. If the light's wavelength is cleverly adapted to the choice of atoms, these can be trapped and moved by manipulating the light field geometry [7]. In the case of cesium atoms it is even possible to achieve a differential coupling based on the internal spin state, which allows state-dependent transport of the atoms [13]. The states considered in the 1D Quantum Walk experiment are the $|3,3\rangle$ and $|4,4\rangle$ hyperfine levels of the cesium ground state. During quantum experiments, the qubit created by these states can be manipulated through application of microwave pulses, on resonance with the $|3,3\rangle \leftrightarrow |4,4\rangle$ transition frequency. Using quantum walks and atom interferometers, made up of both transport steps and microwave pulses of different duration, other physical processes can be simulated [13].

2.1 Atom-light interaction

If an atom is placed in a light field, the electric field $\vec{E}(\vec{r},t) = \frac{1}{2}(\vec{E}_0(\vec{r})e^{-i\omega t} + c.c.)$ of the incident light induces an optical dipole moment $\vec{d}(\vec{r},t)$ in the atom that oscillates at the driving frequency of the light field ω_L. This can be described semi-classically by assuming the atom as a quantum mechanic two-state system (consisting of an excited $|e\rangle$ and a ground state $|g\rangle$) interacting with a classical light field [11].

For small intensities of the light field, the induced dipole moment depends linearly on the electric field: $\vec{d}(\vec{r}) = \alpha(\omega_L)\vec{E}(\vec{r})$. The proportionality is given by $\alpha(\omega_L)$, the complex polarizability, which depends on the internal state of the atom and the frequency of the light [7]:

$$\alpha(\omega_L) = \frac{e^2}{m_e}\frac{1}{\omega_0^2 + \omega_L^2 - i\omega_L\Gamma} \tag{1}$$

Here ω_0 is the atomic resonance frequency, and Γ describes the spontaneous decay of a given initial state into a different final states; it can be calculated using Fermi's golden rule. Thus we get a relationship between the state's lifetime, and it's atomic polarizability and dipole moment [15]:

$$\Gamma = \frac{\omega_0^3}{3\pi c^3 \epsilon_0 \hbar} |\langle e|\vec{d}|g\rangle|^2. \tag{2}$$

The Cs $6^2S_{\frac{1}{2}} \rightarrow 6^2P_{\frac{3}{2}}$ transition has a decay rate of $\Gamma = 2\pi \cdot 5.23\,\mathrm{MHz}$ [12]. Here $6^2S_{\frac{1}{2}}$ is the cesium ground state, written in the standard spectroscopy notation $n^{2S+1}L_J$.

This can be used to obtain formulae for the experimentally relevant expressions. The optical dipole force is conservative and can be derived from a potential: in case of an optical dipole trap (see section 2.3), the trap depth is the same as the dipole potential, which also corresponds to a shift of the atomic energy levels commonly known as the AC Stark shift (see section 2.5) [7]:

$$U_{\mathrm{dip}}(\vec{r}) = -\frac{1}{2} < \vec{d}\vec{E} > = -\frac{1}{2} < \alpha(\omega)\vec{E}^2 > = -\frac{3\pi c^2}{2\omega_0^3}\frac{\Gamma}{\Delta} I(\vec{r}). \tag{3}$$

When $\Delta < 0$ ($\omega_L < \omega_0$) the dipole potential is negative and the atoms are attracted to intensity maxima of the light field. This is also called red-detuning; for blue-detuned light ($\Delta > 0$) the atoms are correspondingly repulsed by the light field.

The absorptive part of the dipole interaction leads to inelastic scattering of the photons of the trapping light [7]:

$$\text{Scattering Rate: } \Gamma_{\mathrm{scat}}(\vec{r}) = \frac{3\pi c^2}{2\hbar\omega_0^3}(\frac{\Gamma}{\Delta})^2 I(\vec{r}). \tag{4}$$

As seen in equations 3 and 4 the dipole potential scales as I/Δ, whereas the scattering scales with I/Δ^2. Therefore often large detunings (for example ND:YAG laser with $\lambda = 1064$nm) are used in other experiments [7]. However, the 1D Quantum Walk experiment requires state-dependent transport, and to this end a frequency which enables a differential coupling of our Cs hyperfine states to the light field is needed.

2.2 Cesium

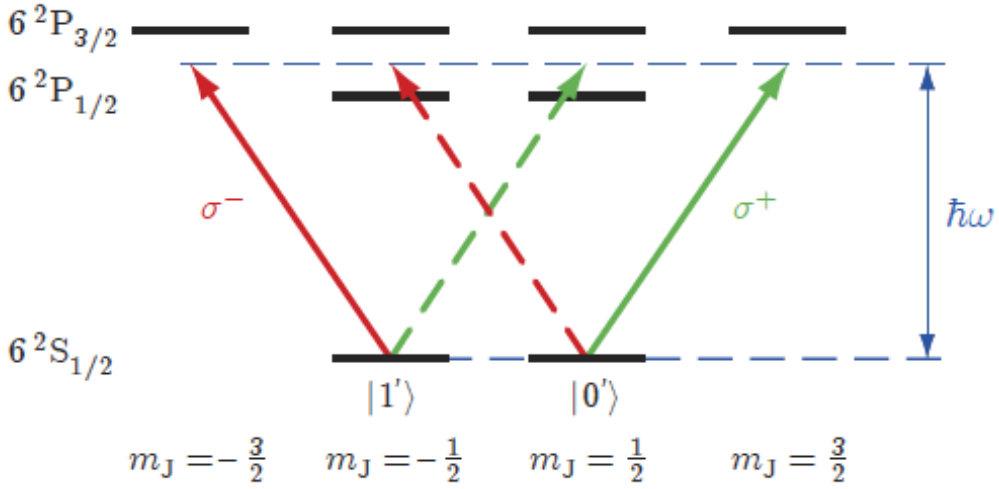

Figure 1: Term diagram of the fine-structure of the ground and first excited states of cesium. Shown are possible transitions for circularly polarized light.

In the experiment the hyperfine states $|F = 4, m_F = 4\rangle$ and $|F = 3, m_F = 3\rangle$ of the cesium ground state are used. In a most correct calculation of the atomic polarizability one should take into account all possible cesium transitions. However, in this case it suffices to take into account only the strongest two transitions: the D_1 and D_2 lines [17]. The D_2 line at 894.6 nm corresponds to the $6^2S_{\frac{1}{2}} \leftrightarrow 6^2P_{\frac{3}{2}}$ transition; the D_1 line at 852.3 nm to $6^2S_{\frac{1}{2}} \leftrightarrow 6^2P_{\frac{1}{2}}$ [12]. The effective detuning is given by [7]:

$$\frac{1}{\Delta_{\text{eff}}} = \frac{1}{3}\left(\frac{1}{\Delta_{D1}} + \frac{2}{\Delta_{D2}}\right). \tag{5}$$

If the atoms are exposed to a linearly polarized light field that is detuned between the D_1 and D_2 line, the $|F = 3\rangle$ and $|F = 4\rangle$ states will couple to both via the σ^+ and σ^- contributions of the light (see Fig. 1). They are red-detuned with respect to the D_2 line, the $J = \frac{1}{2} \rightarrow J' = \frac{3}{2}$ transition, which forms an attractive potential (see Fig. 1). However, in respect to the $J = \frac{1}{2} \rightarrow J' = \frac{1}{2}$ transition they are blue-detuned, yielding a repulsive potential. By detuning the light field near to the middle of the D_1 and D_2 line the attractive and the repulsive contributions from the $m'_J = \pm\frac{1}{2}$ transitions cancel each other out. The uncompensated attractive forces from the outermost states $|J' = \frac{3}{2}, m'_J \pm \frac{3}{2}\rangle$ form the state-selective (re-detuned) potentials, in which atoms of the different fine-structure levels are trapped state-dependently [18].

The $|3, 3\rangle$ and $|4, 4\rangle$ are composed of [18]:

$$\begin{aligned} |4,4\rangle &\widehat{=} \left|m_I = \frac{7}{2}, m_S = \frac{1}{2}\right\rangle \\ |3,3\rangle &\widehat{=} \sqrt{\frac{7}{8}}\left|m_I = \frac{7}{2}, m_S = -\frac{1}{2}\right\rangle - \sqrt{\frac{1}{8}}\left|m_I = \frac{5}{2}, m_S = \frac{1}{2}\right\rangle. \end{aligned} \tag{6}$$

Therefore $|4, 4\rangle$ can couple only to $|J' = \frac{3}{2}, m'_J = \frac{3}{2}\rangle$ via σ^+ light, however $|3, 3\rangle$ will be coupled by both σ^+ and σ^-. Hence it is theoretically impossible to obtain a completely independent coupling of the

light field to the m_F-states. Nonetheless two 'magic' wavelengths exist, for which either $|4,4\rangle$ or $|3,3\rangle$ couples to but one circular polarization. These can be calculated by minimizing the $\sigma^{+/-}$-dependent part of the dipole potential $U_{4/3}$. In the first version of the set-up, there were experimental reasons to minimize for $|4,4\rangle$: one then obtains a wavelength of $\lambda = 865.9$nm for the trapping field [18]. The resulting state-dependent potentials are:

$$\begin{aligned} U_4 &= U_{\sigma^+} \\ U_3 &= \frac{7}{8}U_{\sigma^-} + \frac{1}{8}U_{\sigma^+} \end{aligned} \tag{7}$$

2.3 Light field geometry and transport

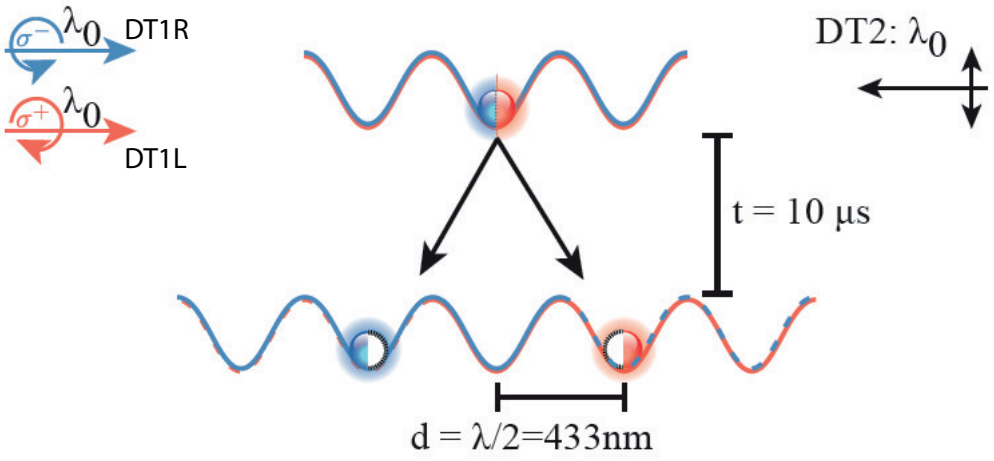

Figure 2: The principle of state-dependent transport

The optical dipole force can be used to trap ultracold atoms in specific light field geometries. One such system is the standing wave dipole trap: two linearly polarized, counter-propagating gaussian laser beams create a standing wave when overlapped in the longitudinal direction. In our system only one of the dipole trap beams (Dipole Trap 2: DT2; see Fig. 2) is linearly polarized, the other (DT1) consists of two superimposed, independently operated, σ^+- and σ^--polarized beams (DT1L and DT1R respectively)[1]:

$$I_{tot} = \frac{c \cdot \epsilon_0}{2} \cdot |\vec{E}_{DT2} + \vec{E}_{\sigma^+} + \vec{E}_{\sigma^-}|^2 \tag{8}$$

$$I_{tot} = I_0 \cos^2(kz). \tag{9}$$

A standing wave, with a power of P/2 in each beam, and a beam waist w_0, yields [17]:

$$I_0 = \frac{4P}{\pi w_0^2}. \tag{10}$$

The DT1 and DT2 beams have a typical waist of 20 µm and intensities of 30mW for the deep or 6mW for the shallow lattice respectively. The deep lattice is used to capture the atoms, the shallow one for experiments - we ramp between these two adiabatically [16].

In the experiment the standing wave passes through a vacuum cell that contains the cesium atoms. Using a Magneto-Optical-Trap (MOT) the atoms are cooled, before they can be 'loaded' into the dipole trap [10, 15, 17]. As soon as they are cool enough the atoms sense the light field, and are attracted to the maxima of its intensity. As a result they are fixed to the 1D optical lattice sites

[1] see chapter 5 for a more extensive description of our experimental set-up

(periodicity: $\frac{\lambda}{2} = 433\text{nm}$). Additionally they can be controlled dynamically by shifting the phase between DT1 and DT2 to achieve an optical conveyor belt, or between the circular polarizations for state-dependent transport [8, 9, 18].

This transport is what enables quantum walk and atom interferometer experiments [13]. If the relative phase between the σ^+ and σ^- beams is shifted by $\alpha = \pi$ the lattices are moved one lattice site apart.

2.4 Measurement

At the beginning of an experiment the atoms are prepared in the $|4, 4\rangle$ state. During the experiment the relative distribution of the $|4, 4\rangle$ and $|3, 3\rangle$ states can be manipulated by applying microwave pulses with the transition frequency $\omega_{\text{hfs}} = 9.2\,\text{GHz}$ to the ensemble. Depending on the length of the pulse we can prepare an arbitrary superposition of the two states, and by combining pulses, transport, push-out, and normal time evolution, a range of experiments is possible. The push-out, microwave pulses and detection each have a fidelity better than 95 %.

To image the atoms, fluorescence detection is used [10]. During an imaging step we continuously drive the $F = 4 \rightarrow F = 5$ transition: it is approximately closed, which means that the atoms fall back to $F = 4$ almost exclusively, from where they are repumped into $F = 5$. While falling back the atoms re-emit a photon, with the same probability in all spatial directions. These fluorescence photons are then collected with an objective and measured with a CCD camera ($\approx$ a few thousand fluorescence photons per atom per picture).

2.5 Light shifts

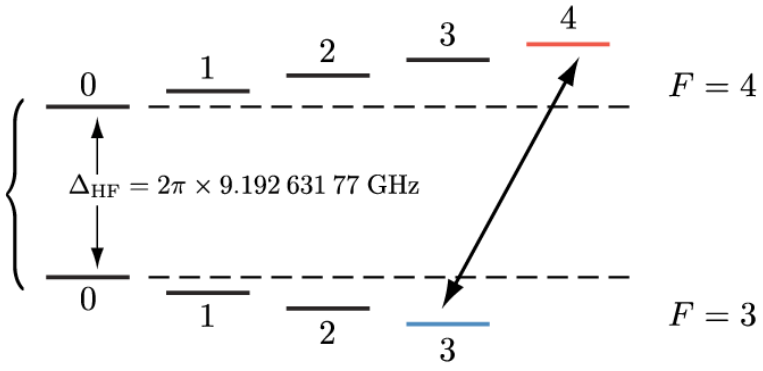

Figure 3: Term diagram of the m_F hyperfine levels of the cesium ground state.

Since all information about the internal states of our system is manipulated and/or extracted by applying microwave pulses that are on resonance with the $|3, 3\rangle \leftrightarrow |4, 4\rangle$ transition ω_0, a precise knowledge of this transition frequency is essential for performing coherent quantum experiments. The frequency is altered both through Zeeman shifts of the energy levels caused by external magnetic fields, as well as differential AC Stark shifts caused by oscillating electric fields. The latter is also called differential light shift and describes the optically induced shift of the ground state as well as the excited state (in the opposite direction) caused by the dipole potential [17].

The prerequisite splitting of the hyperfine states is achieved by applying homogeneous external magnetic fields, lifting the degeneracy of the ground state by a Zeeman shift of the energy levels. The magnetic field also provides a quantization axis for the experiment. The $|F = 3\rangle$ and $|F = 4\rangle$ hyperfine states are separated by 9.19 GHz[2], and in this case the m_F levels are splitted by an additional shift of 7.3 MHz (see Fig. 3). However, this shift causes our qubit states to couple to the D_1 and D_2 with

[2]This value is exact, since it is the basis for the SI definition of the second.

different strength: the detuning of the light field is $\omega_{\text{hfs}} = 9.2\text{GHz}$ less for an atom in $|F = 4, m_F = 4\rangle$ than for one in $|F = 3, m_F = 3\rangle$. As a consequence the $|4, 4\rangle$ level experiences a slightly stronger light shift, resulting in a shift of the $|3, 3\rangle \leftrightarrow |4, 4\rangle$ transition towards smaller resonance frequencies. The resulting scalar differential light shift δ_0 can be approximated as [15]:

$$\delta_0 = \frac{1}{\hbar}(U_0(\Delta_{\text{eff}}) - U_0(\Delta_{\text{eff}} + \omega_{\text{hfs}})). \tag{11}$$

With an effective detuning of $\Delta_{\text{eff}} = -1.2 \cdot 10^7\,\Gamma$. Since $w_{\text{hfs}} \ll \Delta_{\text{eff}}$, the differential light shift is:

$$\delta_0 = \frac{1}{\hbar}\frac{\omega_{\text{hfs}}}{\Delta_{\text{eff}}}U_0. \tag{12}$$

Thus the scalar differential light shift is proportional to the total optical potential with a scaling factor of $\eta = \frac{\omega_{\text{hfs}}}{\Delta_{\text{eff}}} = 1.45 \cdot 10^{-4}$.

In general, the differential light shift depends on the polarization of the light field. In the case of linearly polarized light the contribution of the vector polarizability to the AC Stark shift is zero and these shifts are called scalar light shifts. Vector light shifts are those sensitive to the polarization of the photons: they occur in case of circularly polarized light [14]. Only differential light shifts will change the transition frequency between the $|3, 3\rangle$ and $|4, 4\rangle$ states:

$$\Delta_{\text{diff}}(\vec{r}) = \frac{1}{\hbar}(U_4(\vec{r}) - U_3(\vec{r})). \tag{13}$$

Where the potentials are given by:

$$\begin{aligned} U_4 &= (1 + \frac{1}{2}\frac{\eta}{\hbar})U_{\sigma^+} \\ U_3 &= (1 - \frac{1}{2}\frac{\eta}{\hbar})(\frac{7}{8}U_{\sigma^-} + \frac{1}{8}U_{\sigma^+}) \\ U_0 &= U_{\sigma^+} + U_{\sigma^-} \end{aligned} \tag{14}$$

A difference between the U_{σ^+} and U_{σ^-} potentials results in an ≈ 850 times stronger differential light shift than a shift of U_0 by the same amount.

3 Decoherence

In a perfectly isolated two-level quantum system the time evolution is unitary and thus reversible. However, for realistic qubits some coupling to the environment is inevitable. This coupling causes decoherence, i.e. the evolution of the pure quantum state into a statistical mixture of states, which corresponds to an effective loss of the information stored in the qubit [11]. The characteristic timescale on which the state is preserved to a fraction 1/e of its original value is called the coherence time: only within this time the system retains its quantum behavior and meaningful quantum experiments can be performed. As such, it is important to determine the coherence time precisely and identify the underlying decoherence mechanisms. Due to the probabilistic nature of quantum mechanics, one has to observe atoms in an ensemble average. Decoherence in this case is caused by a decay or dephasing of the induced magnetic dipole moments within the $|3,3\rangle$ and $|4,4\rangle$ superposition state.

The decay rates can be included in the optical Bloch equations as dampening terms, which yields a notation of the characteristic population and polarization decay times similar to the one used for nuclear magnetic resonance [11]:

The *longitudinal relaxation time* T_1, also called population decay time, describes the decay of the population to a stationary value. Its duration depends solely on scattering effects by photons of the optical lattice's light field which couple the two hyperfine states via a two-photon Raman transition. This effect is suppressed due to destructive interference, and scales with I/Δ^4 [5, 15]. It will not be considered here, since our T_1 time of 100 ms is approx. 500 times bigger than the T_2 time - yielding it effectively irrelevant for our experiments.

The *total transverse relaxation time* T_2, also called the polarization decay time, describes the dephasing of the induced electric dipole moment (the polarization) of the atoms. These transversal dephasing mechanisms are divided into two main categories: homogeneous and inhomogeneous dephasing. Homogeneous dephasing affects each qubit of the ensemble in the same way, whereas inhomogeneous dephasing only occurs in the case of an ensemble of qubits each evolving at slightly different resonance frequencies. The dichotomy is useful because constant inhomogeneous dephasing can be cancelled, whereas homogeneous dephasing can not.

$T_2^{'}$: *homogeneous dephasing* results from a homogeneous differential light shift δ during the time of the experiment. Intensity and phase fluctuations, and pointing instabilities[3] of the light field generating the optical lattice, as well as fluctuations of the magnetic field, play into this effect.

T_2^*: *inhomogeneous dephasing* is caused by the distribution of individual atomic resonance frequencies, which depends on their environment and thermal energy. Due to these different resonance frequencies the atoms lose their relative phase relationship, which results in a macroscopic dephasing because of ensemble averaging. In our case the inhomogeneous dephasing is dominated by the thermal distribution of the trapped atoms: depending on their energy the atoms see a different trap depth, which results in a distribution of the accumulated phase [11]. The total transverse relaxation time is related to the homogeneous dephasing time $T_2^{'}$ and the reversible inhomogeneous dephasing time T_2^* via [11]:

$$\frac{1}{T_2} = \frac{1}{T_2^{'}} + \frac{1}{T_2^*}. \tag{15}$$

The independent treatment of the various decay mechanisms is justified by the very different timescales of these processes: $T_1 \gg T_2^{'} \gg T_2^*$ [15]. In the rest of this thesis all fluctuations will be considered independently.

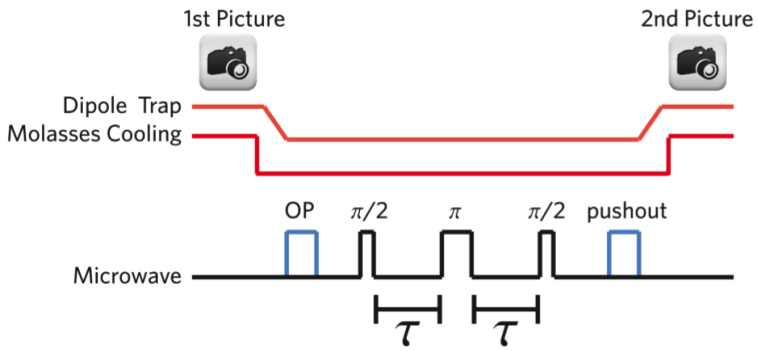

Figure 4: Ramsey with spin echo; OP stands for optical pumping of the $|4,4\rangle$ state

3.1 Ramsey contrast and spin echo visibility

To gain information about the time evolution of our superposition state's phase we employ Ramsey phase spectroscopy [13, 18]. It is based on the application of two rectangular, resonant (microwave) $\frac{\pi}{2}$ pulses, with a relative phase of ϕ_{MW}, separated by a time τ (see Fig. 4). The first pulse creates a 50/50 superposition state of $|3,3\rangle$ and $|4,4\rangle$: $\frac{1}{\sqrt{2}}(|4,4\rangle + e^{i\phi}|3,3\rangle)$. This precesses along the equator of the Bloch sphere, with an angular frequency δ depending on the atomic transition frequency. The second pulse then projects the superposition onto the w-axis of the Bloch sphere, where the population in the $|F=4\rangle$ state is imaged. By scanning the relative phase ϕ_{MW} of the $\frac{\pi}{2}$ pulses, we map the phase of the ensemble: such an image is called a Ramsey Fringe. Through combination of many Ramsey Fringe images for different values of τ, the time evolution of the Ramsey contrast $C(\tau)$ can be measured. By studying the Ramsey contrast we can gain insight into the dephasing and the T_2 time of our ensemble.

The probability to find a particle in $|F=4\rangle$ is given by [13, 18]:

$$P_{|F=4\rangle}(\tau) = \frac{1}{2}(1 + C(\tau)\cdot\cos(\phi_{MW} + \phi(\tau))). \tag{16}$$

Here $\phi(\tau)$ is the phase collected during τ

$$\phi(\tau) = \int_0^\tau \delta(t)dt \tag{17}$$

Due to dephasing, the contrast $C(\tau)$ of a Ramsey phase scan decays as a function of time τ. This decay is dominated by inhomogeneous dephasing: its envelope is the Fourier-transformation of the atomic energy distribution [11, 15]. However, there are methods to counteract inhomogeneous dephasing effects: a spin echo sequence is a Ramsey sequence with an additional π-Pulse midway (at τ_{SE}) between the two $\frac{\pi}{2}$ pulses. This flips the states by 180°, and causes them to precess in the opposite direction. As such, differential phases which are effectively constant during τ_{SE} are eliminated [1]. This only works for deviations that are either constant on the time-scale of the spin echo, or fluctuate so quickly that they are averaged over time and can be seen as effectively constant (in that case the effects of the last oscillation period are not countered, but these will be small). Fluctuations that take place on the same time scale as the spin-echo pulses are impossible to null with this method. In our case, the time used for a spin-echo step is typically 20 µs, therefore inhomogeneous fluctuations with a frequency of ≈ 50 kHz will have most impact on the system. Such irreversed dephasing manifests itself in the decay of spin-echo visibility, together with homogeneous dephasing. Spin-echo visibility is the analogue of Ramsey contrast: the effectivity of the spin-echo pulse decreases as the time τ_{SE} increases.

[3] Changes in the relative position of the trapping beams, that arise due to variations of the optic path, will influence the interference contrast in the trap and thus the light shift [11]. The pointing instabilities will not be considered separately in the remainder of this thesis.

If one assumes a gaussian distribution of the accumulated phases, $p(\phi(\tau)) = \mathcal{N}(0, \sigma_{\phi(\tau)})$ where $\sigma_{\phi(\tau)} = \sigma_{\text{fluc}}\tau$, the spin-echo visibility V is given by [11]:

$$\begin{aligned} V(\tau) &= C_0 \int d\phi(\tau) \cos(\phi_{MW} + \phi(\tau)) p(\phi(\tau)) \\ &= C_0 \int d\phi(\tau) \cos(\phi_{MW} + \phi(\tau)) \frac{1}{2\pi\sigma^2_{\phi(\tau)}} e^{-\frac{\phi(\tau)^2}{2\sigma^2_{\phi(\tau)}}} \\ &= C_0 \cos(\phi_{MW}) e^{-\frac{\sigma^2_{\phi(\tau)}}{2}} \\ &= C_0 \cos(\phi_{MW}) e^{-\frac{1}{2}\tau^2\sigma^2_{\text{fluc}}}. \end{aligned} \tag{18}$$

$$V(T_2') = C_0 e^{-1} \Rightarrow T_2' = \frac{\sqrt{2}}{\sigma_{\text{fluc}}} \tag{19}$$

Therefore we can predict the homogeneous T_2' time, based on knowledge of the RMS value of the combined homogeneous fluctuations. However, since the detuning is not constant, equation 19 is only truly predictive if the used RMS value is an average over many, measured at different moments in time.

4 Noise

From the previous chapters we can surmise that a thorough understanding of our dephasing noise is needed to explain and even predict our decoherence time. Noise, in its widest sense, stems from any experimental parameters deviating from their ideal value. Specifically, we are only interested in noise that induces a differential light-shift: an uncertainty of ω_0 will directly translate into an uncertainty of $\phi(t)$, and thus into dephasing. In this chapter different kinds of noise are considered, and their influence on our atoms. In the entire chapter all inhomogeneous effects are assumed to be counteracted; the considered homogeneous fluctuations include intensity and phase noise, as well as fluctuations of the magnetic field. In general the strongest dephasing effects are caused by vector differential light shifts, which occur due to an imbalance between the σ_+ and σ_- lattices. These effects that degrade the purity of the synthesized polarization, as characterized by the minimal extinction ratio, will be studied to a greater extent in section 4.2.

4.1 Fluctuations

Since constant experimental imperfections are absorbed into the definition of the $|3,3\rangle \leftrightarrow |4,4\rangle$ transition frequency, dephasing comes solely from fluctuations of our experimental values. It is useful to categorize these fluctuations based on the amount of correlation between them: we differentiate between common mode (CM) and non-common mode (NCM) fluctuations upon our trapping beams. Within the set-up there are three beams we have to take into account: DT2, and DT1L and DT1R, where the last two are combined to form DT1. Although the light comes from the same laser source, the three beams take different optical paths and the intensity and phase of DT1L and DT1R are independently electronically stabilized, with the result that we have both CM and NCM noise portions on all beams.

The noise can be described by its root-mean-square (RMS) value, or its power spectral density (PSD). The RMS is an effective value for the magnitude of the variation from our desired value. The PSD however, gives information about the power of the noise at distinct frequencies. Proper knowledge of the frequency of noise is relevant for both homogeneous and inhomogeneous dephasing: by measuring the PSD, or calculating the RMS for a distinct bandwidth, we can find out the magnitude of the fluctuations that influence our atoms during a sequence of a specific length T. Though the atoms will not be effected by very fast fluctuations because these average out statistically, slower fluctuations and drifts, a monotonous increase or decrease on the time-scale of the experiment, are irreversible. The biggest effect is seen by fluctuations on the time-scale of the experimental sequences. Therefore, when describing the dephasing, the gaussian distribution of the detunings should be weighted in regard to the sequence-time[4]. Additionally, insight in the PSD might serve as a method to distinguish different types of noise: it offers a way to determine the correlation between noise on different beams (CM vs. NCM), and it gives an indication of peak frequencies associated with distinct noise sources. In equation 18 the phase resulting from time-dependent homogeneous fluctuations was assumed to follow a gaussian distribution. By assuming a gaussian distribution of phases, we have assumed a gaussian distribution of the underlying noise. The assumption of gaussian noise is prompted whenever one describes serially uncorrelated random variables with zero mean and finite variance. Thus it seems a valid description for intensity and phase fluctuations caused by the laser. However, we also have other forms of noise in addition to this (shot noise, flicker noise). In general we can describe the collected differential phase during our Ramsey phase scan as:

$$\phi_T(\tau) = \frac{1}{\hbar}\int_0^T \delta(\tau + t)dt \tag{20}$$

$$= \frac{1}{\hbar}\int_{-\infty}^{\infty} X_T(\tau - t')\delta(t')dt' = \frac{1}{\hbar}(X_T * \delta)(\tau) \tag{21}$$

[4]Not only the time of the experimental sequence, but also the time between two repetitions of sequences (shot-to-shot time) should be regarded.

Where X is a rectangular window function from $[-\frac{T}{2}+\tau, \frac{T}{2}+\tau]$:

$$X = \text{rect}(\frac{t+\tau}{T}) \tag{22}$$

$$\mathscr{F}(X_T)(\omega) = \frac{1}{\sqrt{2\pi}}\int_{-\infty}^{\infty} \text{rect}(\frac{t+\tau}{T})\exp(-i\omega t)dt = \frac{1}{\sqrt{2\pi}}\text{sinc}(\omega\frac{T}{2}) \tag{23}$$

$$\mathscr{F}(\delta)(\omega) = \frac{1}{\sqrt{2\pi}}\int_{-\infty}^{\infty} \delta(t)\exp(-i\omega t)dt \tag{24}$$

The power spectral density is defined as:

$$S_{\delta(t)} = \lim_{T\to\infty}\frac{1}{T}|\mathscr{F}(\delta(t))(\omega)|^2 \tag{25}$$

With the result that we can express the variation of our phase as:

$$\begin{aligned}\sigma_\phi^2(T) = \langle\phi_T^2\rangle_\tau &= \lim_{\mathscr{T}\to\infty}\frac{1}{\mathscr{T}}\frac{1}{\hbar^2}\int_{-\frac{\mathscr{T}}{2}}^{\frac{\mathscr{T}}{2}}(X_T * \delta)^2(\tau)d\tau \\ &= \lim_{\mathscr{T}\to\infty}\frac{1}{\mathscr{T}}\frac{1}{\hbar^2}\int_{-\infty}^{\infty}\frac{d\omega}{2\pi}|X_T(\omega)|^2\cdot|\delta(\omega)|^2 \\ &= \frac{1}{\hbar^2}\int_{-\infty}^{\infty}\frac{d\omega}{2\pi}\text{sinc}^2(\omega\frac{T}{2})\cdot S_{\delta(t)}\end{aligned} \tag{26}$$

By measuring the PSD of the detuning, $S_{\delta(t)}$, one can estimate the relative influence of different experimental parameters on decoherence. However, in the current set-up this has only been done for the phase noise so far.

4.1.1 Intensity noise

Fluctuations of the laser beam intensity directly effect the trap depth and thus the homogeneous dephasing of our atoms. NCM fluctuations between σ_+ and σ_- will create vector differential light shifts, whereas CM fluctuations contribute only to scalar differential light shifts (see equation 12).

4.1.2 Phase noise

A shift in phase can be equated with a transport step. A phase between DT1 and DT2 will shift the trap; between DT1R and DT1L will shift the potentials. Phase noise can be described in the time domain if one uses the Allan deviation, or else by using the power spectral density in the frequency domain [3, 19].

Common mode phase fluctuations between DT1 and DT2 will cancel out. NCM fluctuations between DT1 and DT2 on the other hand, will cause the entire trap to jiggle along the longitudinal direction. If there are inhomogeneous effects that depend on the absolute position of an atom, such as magnetic field gradients, the $\text{NCM}_{1\leftrightarrow 2}$ phase fluctuations will introduce time-dependent inhomogeneous dephasing. In general, $\text{NCM}_{1\leftrightarrow 2}$ could be problematic if one has to target lattice sites at an absolute position in space. However these fluctuations lead to only 60 pm displacement, whereas the lattice sites are 433 nm.

$\text{NCM}_{L\leftrightarrow R}$ phase noise will shift the σ_+ and σ_- lattices apart. Since $|3,3\rangle$ sees a different lattice than $|4,4\rangle$, the noise induces an intensity modulation of the $|3,3\rangle$ lattice and thus a vector differential light shift.

We measured the PSD of the ($\text{NCM}_{1\leftrightarrow 2}$) phase noise in our set-up: it proved to be mostly non common mode. The error signal was calibrated in angle units, and it turned out that the RMS phase noise is

quite low: it is on the order of $\Delta\phi = 1/20$ of a degree. This would correspond to an RMS value of maximally

$$2 \cdot \frac{\cos(\pi + \Delta\phi) + 1}{180} = 2 \cdot \frac{\cos(\pi + 1/20) + 1}{180} \\ = 1.2 \cdot 10^{-5}$$

when measuring the minimal extinction ratio (see section 4.2).

4.1.3 Magnetic fields

The magnetic fields used to lift the degeneracy of the cesium ground state may also fluctuate in time, and can cause a differential shift of the energy levels. Fluctuations of the magnetic guiding field are caused by noise on the driving current in the coils used for its production. They are $<$ 1kHz [18]. An estimation of the magnetic dephasing effects has been made by measuring the T_2 time with switched-off dipole trap. In this case the atoms start falling because the earth's gravitational field is no longer compensated, however the resulting displacement is sufficiently small to measure the T_2 time without light-induced dephasing, before the atoms move out of the trap. We achieved a T_2 time of 400 µs: approx. 3 times longer than the current T_2 time. As such it seems we are currently limited by other sources of dephasing, and I will not consider the influence of magnetic fields any further.

4.2 Minimal extinction ratio

We trap our atoms state-dependently with σ^+ or σ^- light. Differences in phase, intensity or the transverse profile of the σ^+/σ^- beams cause a difference in the trapping lattices, which we shall call polarization impurity, and create a vector differential light shift. The indicator of choice for the polarization purity is the minimal extinction ratio. It is given by:

$$\epsilon_{min} = \frac{I_{min}}{I_{max}}. \tag{27}$$

Where I_{min} and I_{max} denote the minimal and maximal light intensity in a beam behind a linear polarizer. An extinction ratio of 0 means that the incident light is perfectly linearly polarized: we would like to come as close to 0 as possible. In the previous version of the set-up, which used an electro-optic modulator (EOM) instead of acousto-optic modulators (AOMs) for polarization synthesis (see section 5 for a description of the set-up), the extinction ratio was $4 \cdot 10^{-4}$ with bests of $2.5 \cdot 10^{-4}$. Our current set-up is already slightly better, at $1 \cdot 10^{-4}$.

There are several things that can cause an imperfect minimal extinction ratio, $\epsilon_{min} > 0$:

- DT1L and DT1R are not purely σ^+ or σ^- respectively, rather they are contaminated with some of the other polarization
- DT1L and DT1R differ in intensity
- DT1L and DT1R differ in phase
- DT1L and DT1R's wavefront and transverse coordinates are imperfectly overlapped.

The NCM fluctuations in phase and/or intensity of DT1L and DT1R cause the AC component of the minimal extinction ratio: the measured value of these fluctuations is therefore an upper bound of the NCM phase/intensity noise in our system. The DC value of the minimal extinction ratio can be equated with a defilement of the two orthogonal polarizations. It is created by imperfections of components in the beam, such as wavefront errors in waveplates and birefringence in the fiber. The resulting imbalance in the strength of the σ^+ and σ^- lattice causes a vector differential light shift. If the system is at rest, a static change in the transition frequency between $|3,3\rangle$ and $|4,4\rangle$ due to crosstalk will be incorporated in the 'zero' transition frequency. This changes in the case of atom transport: due to the contamination the σ^+/σ^- lattices can not be moved perfectly independently, which introduces an extra intensity modulation of the lattice as seen by the different states.

Additionally, such static polarization contamination will bring about phase and intensity fluctuations in the set-up, due to the stabilization loops. Since the ILL or PLL can influence but one beam, and see but one polarization, static polarization crosstalk will appear as noise in the locked loop. Crosstalk of -40 dB causes phase noise of 0.03 ° [19], which is a significant percentage of our total phase noise (0.05 °).

If $A_{DT1L/R}$ is the amplitude of the DT1L/R beam[5]:

$$\begin{aligned} I_{DT1L} &= \frac{A_{DT1L}}{\sqrt{2}}(\alpha_L \left|\sigma^+\right\rangle + \beta_L \left|\sigma^-\right\rangle) \\ I_{DT1R} &= \frac{A_{DT1R}}{\sqrt{2}}(\alpha_R \left|\sigma^+\right\rangle + \beta_R \left|\sigma^-\right\rangle) \end{aligned} \tag{28}$$

Where $\alpha_L^2 + \beta_L^2 = 1 = \alpha_R^2 + \beta_R^2$ and $\alpha_L \gg \beta_L$, $\beta_R \gg \alpha_R$, then

$$\epsilon_{min} = \frac{1}{\sqrt{2}} \frac{A_{DT1L}(\alpha_L + \beta_L) + A_{DT1R}(\alpha_R + \beta_R)}{A_{DT1L}(\alpha_L - \beta_L) + A_{DT1R}(\alpha_R - \beta_R)}. \tag{29}$$

If we assume that $\beta_L = 0$[6] then we can simplify these equations to:

$$\begin{aligned} \beta_R &= \frac{(1 - \epsilon_{min})(A_{DT1L} + A_{DT1R})}{2} \\ \alpha_R &= \sqrt{1 - \beta_R^2}. \end{aligned} \tag{30}$$

Which would mean we could infer the polarization contamination from values measured at the set-up.

[5] In this calculation I assumed that the linear polarization coincides with the x-axis, and the minimal intensity is therefore measured along the y-axis (orthogonal polarization); this polarization vector may be rotated due to phase noise

[6] In general this assumption is not valid: in case of contamination both beams are no longer orthogonal in any reference frame.

5 Set-up

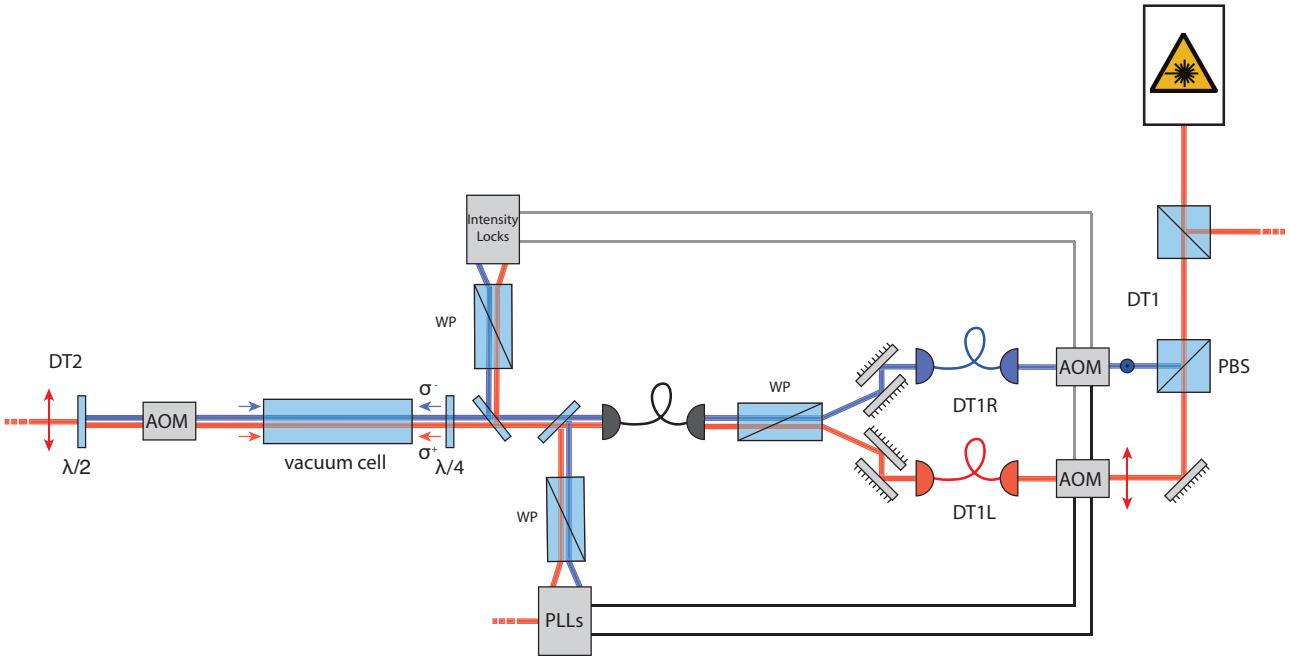

Figure 5: The set-up for direct synthesis of light polarization

Figure 5 shows the experimental set-up. Experiments take place in the vacuum cell, which is held at a pressure of 10^{-10} mbar to minimize scattering of our cesium atoms on background gas. Entering the vacuum cell from the left is the normal linearly polarized beam DT2. From the right comes the synthesized beam DT1, which consists of two superimposed, independently operated, σ^+- and σ^--polarized beams, and is composed of light from the same TiSa as is used for DT2. To create the circularly polarized beams, the beam coming from the TiSa is initially separated in two orthogonal linear polarizations by passing through a polarizing beam splitter (PBS) cube. These beams are entered into acousto-optic modulators (AOMs), which can control both phase and frequency, as well as the amplitude of the beam. The linear polarizations are recombined using a Wollaston Prism. This is then fed into the 'combining fiber', a polarization maintaining (PM) fiber that makes sure both polarizations have the exact same transversal mode before being transformed into σ^+- and σ^--polarized light by a $\frac{\lambda}{4}$ plate. Per beam the fluctuations of phase and amplitude are counteracted by the use of a phase and intensity lock, to which end some light is diverted before the beams proceed into the vacuum cell. There the optical lattice is formed by the counter-propagating beams of DT1 and DT2.

An AOM uses the acousto-optic effect to diffract and shift the frequency of light using sound waves: a piezoelectric transducer driven by a radio frequency (RF) signal creates sound waves in a quartz crystal, which function as a 'diffraction grating' for the incoming laser light. By modulating the intensity, frequency and phase of the RF signal the same parameters of the laser light can be controlled. The response of the AOM is limited by the transit time of the sound wave across the laser beam - it can typically switch within 100 ns - which also sets a limit to the speed of our phase and intensity lock loops (see sections 5.1 and 5.2): our bandwidth is $\approx$ 1MHz.

In our current set-up Wollaston prisms (WP) are used to clean the polarization of the DT1L and DT1R (here still linearly polarized) beams and overlap them into the combining fiber. They are also employed in the intensity and phase lock loops to split the combined beam into its two components. The Wollaston prisms were specially chosen because they combine the a high extinction ratio of 10^{-6}, with a low wavefront distortion in each axis [19]. This extinction ratio is not limiting in our current set-up, since it is 10^2 better than allowed by the combining fiber.

Also the λ-plates used in our set-up do not introduce a significant error. Homogeneous polarization

errors in the waveplates mutually compensate another: with a series of three λ plates it is possible to transfer an arbitrary polarization into an arbitrarily different one. However, if the linear polarizations are not completely orthogonal before the $\lambda/4$-plate, the retardance error of the waveplate will lead to crosstalk between the polarizations [19].

The spatial overlap of DT1 and DT2 is optimized by making sure that the DT2 beam couples into the combining fiber, and counterpropagates throughout the DT1 set-up. The intensity coupled into the fiber is approximately 80 %.

5.1 Phase Lock

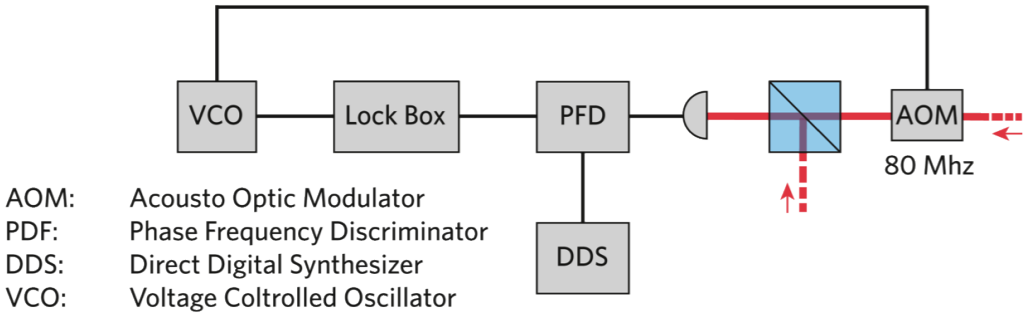

Figure 6: Phase Lock Loop

Phase noise of the σ^+ and σ^- beams is individually stabilized with the help of two separate phase lock loops (PLL). To detect and stabilize the phase and frequency of the σ^+/σ^- light, the laser-light is superimposed by an optical reference beam: the resulting beat-signal is measured by a fast (10 GHz bandwidth) photodiode. The signal is amplified and, to eliminate an amplitude-phase dependency of the signal (introduced by the Schmitt-trigger in the phase frequency discriminator), a limiting amplifier was included in the set-up. The electronic signal from the limiting amplifier is then fed into a phase frequency discriminator (PFD) which detects the difference between the beat-signal and an electronic reference. The electronic reference comes from a direct digital synthesizer (DDS), which enables us to program arbitrary phase and frequency ramps. Subsequently a fast lock box transforms the error signal of the PFD into a control signal for the voltage controlled oscillator (VCO) that drives the AOM (see Fig. 6).

5.2 Intensity Lock

The intensity lock loop (ILL) stabilizes the intensity of the $\sigma^{+/-}$ beams. It utilizes a custom-made, low-noise, photodiode to detect the intensity. After the photodiode subtracts this signal from an electronic one, which can be set with an 'Arbitrary Waveform Generator' from Agilent Technologies, the signal is passed on to the lock box. The error signal from the lock box controls the amplitude of the AOM's RF signal, and thus the intensity of the DT1L and DT1R beams.

5.3 Fiber

As shown in section 4.2, the static polarization purity, measured by the DC value of the minimal extinction ratio, has a significant effect on the decoherence of our quantum states. Currently our biggest limitation in this regard is the optical fiber used to overlap the σ^+ and σ^- components of our beam. The intensity difference between two gaussian beams, as created by a difference of δ in their waist, scales with δ^2. In order to achieve relative intensity differences less than 10^{-4}, we have to overlap our two beams better than 99 %, which proves quite impossible in free space. The fiber

removes this problem, however, it causes a mutual crosstalk between the orthogonal polarizations sent through it.

Currently a single-mode, polarization maintaining (SM-PM) fiber from Thorlabs is built into the set-up. PM fibers maintain the polarization of linearly polarized light that is send through their core, with little cross-coupling of optical power between the polarization modes. The extent of this crosstalk can be quantified with the polarization extinction ratio (PER): when linearly polarized light is sent in, perfectly aligned with the fast axis of the fiber, then all power detected in the orthogonal polarization mode will have been transferred there by cross-coupling processes in the fiber. The fiber we currently use has a PER of $1 \cdot 10^{-4}$, which is much better than specified by the manufacturer. In order to check if all fibers were better than specified, and to see if we had a better fiber, I measured the extinction ratio of several SM-PM fibers: two other Thorlabs fibers with the same specifications, as well as a Schäfter und Kirchhoff fiber with slightly better specifications (specifically bought for this purpose).

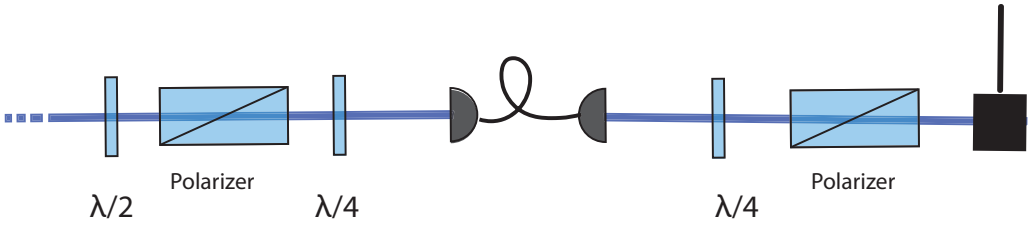

Figure 7: Set-up to measure the extinction ratio of a fiber

For these measurements I used the set-up shown in Fig. 7: light coming from a laser is given a certain polarization axis with help of a $\lambda/2$-plate and a first polarizer. The $\lambda/4$ is used to precompensate a potential elliptic deformation caused by the lens of the fiber in-coupler. The second $\lambda/4$ after the fiber is used correspondingly to compensate the polarization distortions due to the fiber out-coupler. A second polarizer (the analyzer) is used to check the minimal extinction ratio. To be limited solely by the extinction ratio of the fiber, one has to make sure that the two polarizers are of sufficient quality: the codex plates used had an extinction ratio of 10^{-6}. Most PM fibers work by inducing stress in the core: if the polarization of the incoming light is not aligned with the stress direction in the fiber, the output will vary between linear and circularly polarized light, and is highly sensitive to variations in temperature and stress in the fiber. This can be used to find the right axis and thus the true minimal extinction ratio: after a rough first adjustment while looking at the linear extinction ratio, the second polarizer is turned to 45°, the fiber is heated, and the temperature induced fluctuations are minimized by adjusting the first polarizer (and $\lambda/2$-plate). Here should be noted though, that not each fiber mantel reacts to heating in a similar manner. The Schäfter und Kirchhoff fiber seemed to allow for less homogeneous and direct heat transfer than the Thorlabs fibers: for this fiber it was difficult to optimize the minimal extinction ratio with help of the temperature-induced differential phase shift. After the temperature-based optimization, the linear extinction ratio was measured as before.

Fiber	Extinction ratio specified	Experiment
PM Fibers		
Thorlabs PM#001	$5 \cdot 10^{-3}$	$1.2 \cdot 10^{-4}$
Thorlabs fiber PM#002	$5 \cdot 10^{-3}$	$2.4 \cdot 10^{-4}$
Schäfter und Kirchhoff fiber PM#003	$5 \cdot 10^{-4}$	$7.2 \cdot 10^{-5}$
Old DT1 fiber (Thorlabs PM#004)	$5 \cdot 10^{-3}$	$2.5 \cdot 10^{-4}$
SM Fiber		
Thorlabs SM 900 µm	-	$1.6 \cdot 10^{-5}$

Table 1: Fiber extinction ratios

As can be seen in Table 1 it seems that SM-PM fibers are limited to an extinction ratio of approximately 10^{-4}. The experimental limit of PM fibers is at least -52 dB [4], which is higher than what

we currently have built-in. Nonetheless most commercial retailers specify a polarization crosstalk of -40 dB at best, which corresponds to the values I have measured. The best commercial PM fiber I could find was from Nufern: they specified (-48 ± 8) dB for the FUD-3397 PM780-BK-S-BN [20]. This would be slightly better than the current PM fibers, although it would have to be connectorized and polished by ourselves.

5.3.1 The Box

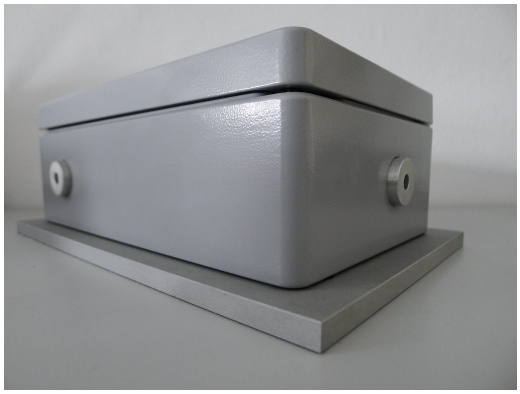

Figure 8: The Box

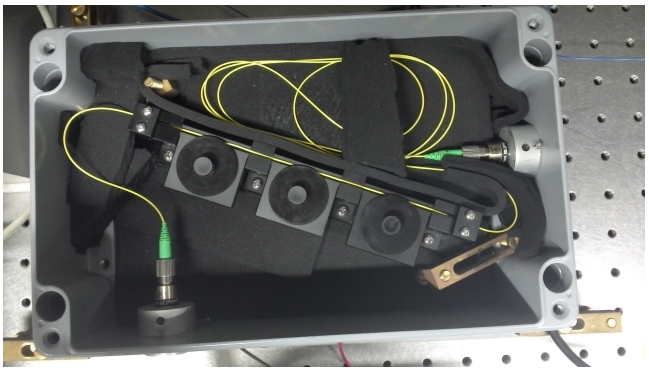

Figure 9: Inside the Box

Buying an alternative PM fiber was but one option we looked into: another possible solution is to investigate the properties of single mode, non polarization maintaining fibers. For this type of fiber a special system can be used instead of normal waveplates: The Manual Fiber Polarization Controller (MFPC) from Thorlabs utilizes stress-induced birefringence to create fiber-internal waveplates. By looping the fiber (1-2-1 times) around three independent spools a series of $\lambda/4$ - $\lambda/2$ - $\lambda/4$ waveplates is created. The fast axis of each plate, which is in the plane of the spool, can be adjusted with respect to the transmitted polarization vector by manually rotating the paddles [21].

The fiber diameter has to be compatible with the MFPC paddles: the used fiber is a custom-ordered 900µm Ø SM Fiber P3-780AR-2 from Thorlabs. Measured in the same way as explained above, the linear extinction ratio seemed almost an order of magnitude better than that of the PM fibers (see Table 1). However, unfortunate though expected, the system was very susceptible to temperature and pressure fluctuations. Therefore I built a temperature stabilized box for the MFPC, loosely securing the fiber inside with EPDM rubber. The fiber collimators are also on the inside and the box is designed so that it does not have to be opened again once the MFPC has been adjusted correctly (see Fig. 8, and 9). The temperature stabilization is achieved by 4 serially connected Peltier elements attached to the underside of the box and a heatsink, in a feedback loop with a temperature sensor and a Thorlabs TED 200C temperature controller. Connected in series to ensure the same current and thus the same cooling properties along the box, 4 Peltier elements proved quite strenuous for the temperature controller: its current had to be limited to 0.2 A so that the voltage would suffice.

While setting up the box and fiber for the stability measurement, it became clear that the fiber had been damaged close to one of the ferrules, possibly during the box's assembly. Given the cost and waiting time associated with ordering a new custom-made fiber, I decided to connectorize and polish the fiber anew. During this process, it turned out that the fiber did not contain an internal layer of protective Kevlar threading, as is customary for 3mm Ø Thorlabs fibers [22]. This is probably the reason for the fiber's fragility, and would be reason to advice against the use of such fibers.

Unfortunately it seems that the new connectorization and set-up had a negative influence on the fiber's minimal extinction ratio: the second measurement of the fiber's minimal extinction ratio yielded values of only $1.6 \cdot 10^{-4}$. This value, and especially this decrease is surprising. Theoretically a SM fiber should have an almost perfect minimal extinction ratio: especially for the length of fiber used here (1 meter), factors such as anisotropic rayleigh scattering within the fiber etc. are negligibly

small. The initial minimal extinction ratio of 10^{-5} was probably limited by impurities within the core or the fiber endfacets. However, homogeneous imperfections of the fiber endfacets, which induce ellipticity in the polarization, should be possible to cancel with waveplates before and after the fiber. Thus the cause of the minimal extinction ratio's deterioration must be sought in the new polishing of the fiber, or the rolled-up configuration of the fiber inside the box, rather than the connectorization alone.

Despite the deteriorated minimal extinction, it was possible to characterize the stabilization of the fiber. To this end the intensity stability in minimal extinction was measured over a longer period of time. A photodiode before the box ('Initial'), after the box and a polarizer ('Final'), as well as a temperature sensor in the box were connected to a MBED, which saved the mean and standard deviation value of these parameters every ten seconds.

First observations seem to indicate a close correlation between the noise on 'Initial' and 'Final' (see Fig. 10). This lack of additional noise after the box suggests that time-dependent crosstalk in the fiber has been effectively reduced. Here it must be noted though, that the stability without the box was not electronically logged over a longer period: because of obvious instability of the fiber, I refrained from such detailed measurements in the initial set-up. Therefore a comparison to previous values is impossible.

A following step in the box's characterization should be a simultaneous measurement of the total intensity in both orthogonal polarizations after the fiber. This would allow to substract effects due to fiber coupling, and retain information about only polarization-dependent fluctuations. It could be achieved by including a glan-laser to split the light into two orthogonal polarizations before the polarizer in the 'Final' measurement. The glan-laser has a minimal extinction ratio of 10^{-6} in one axis, which would not obstruct the measurement of the fiber's minimal extinction ratio. In the other axis the polarization purity might worsen, but a measurement of the total intensity would not be hindered.

Further optimization is also possible in case of the temperature control: no long-term stability (on the order of days) has been achieved yet, since the low maximal current greatly impairs the tunability of the temperature controller. The most recent measurements show strong oscillations over the course of several hours (see Fig. 11). Presumably this is caused by faulty adjustment of the PID controller. If the controller does not prove further tunable, the number of serially connected Peltier elements should be reduced.

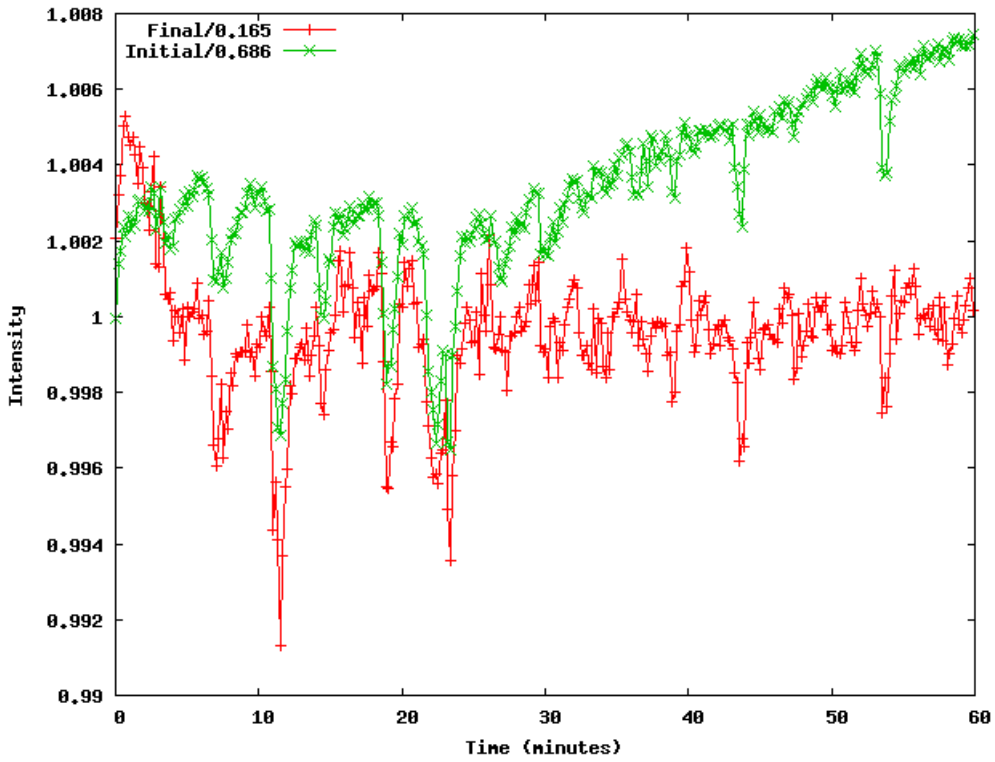

Figure 10: The minimal extinction ratio over the course of 1 hour, during which the temperature was stable to 0.1 %

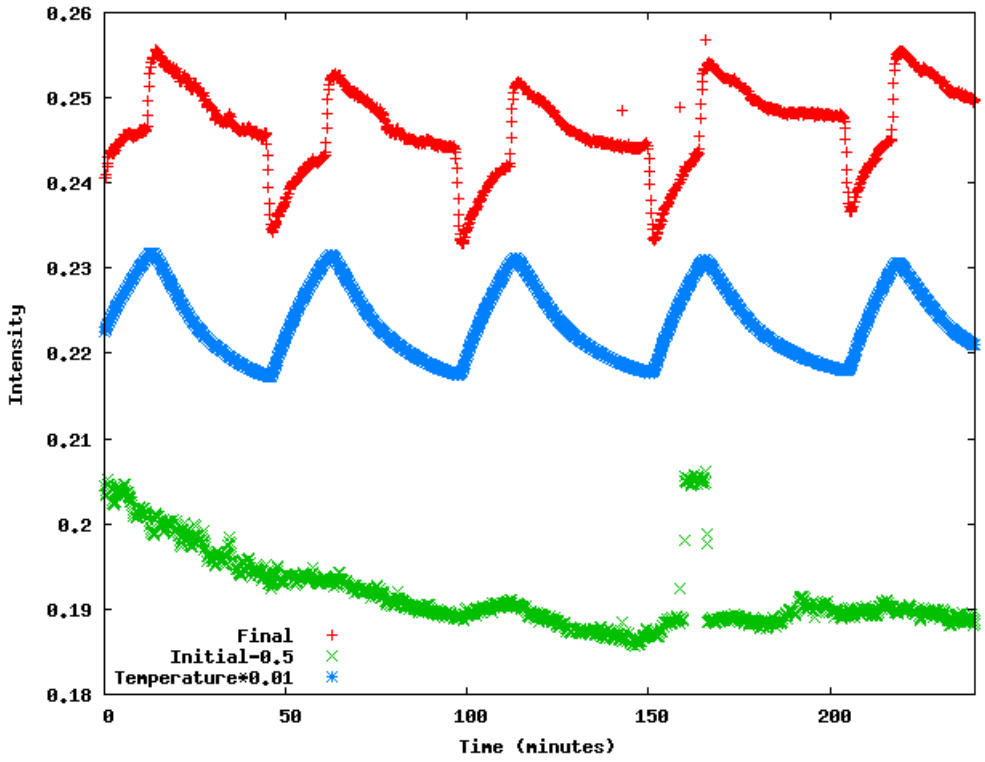

Figure 11: The minimal extinction ratio over the course of 4 hours, after adjustment of the temperature controller

6 Conclusion

We perform quantum experiments with ultracold cesium atoms in a standing wave dipole trap. Utilizing light at $\lambda = 866\,\text{nm}$ atoms are transported depending on their spin state, because they couple to either σ_+ or σ_- components of the light field. This is exploited to conduct quantum walks and single atom interferometers with the qubit formed by the $|F = 3, m_F = 3\rangle$ and $|F = 4, m_F = 4\rangle$ hyperfine levels of the cesium ground state. The qubit can be manipulated with microwave pulses of different length, on resonance with the transition frequency between both states. However, physical processes that shift the energy levels of $|3, 3\rangle$ and $|4, 4\rangle$ will affect the transition frequency. This can be registered as a change in the collected phase of the superposition state as it precesses on the Bloch sphere. If the magnitude of these light shifts is non-predictable, we lose knowledge about the quantum system. The phase relation of the atomic ensemble is lost, and we speak of dephasing.

The dephasing mechanisms are subdivided into homogeneous and inhomogeneous effects, whereby the latter are reversible with the help of spin echo techniques (section 3.1). The homogeneous effects studied in this thesis were primarily the intensity and phase fluctuations of the trapping beams, since the influence of magnetic fields does not limit our current T_2 time. The RMS phase noise is quite low: it is on the order of $\Delta\phi = 1/20$ of a degree; the intensity noise RMS is on the same order of magnitude.

In chapter 5 the current experimental set-up was explained. The phase and intensity noise have been minimized by phase and intensity locks to an RMS value of 10^{-5}. However, other components such as waveplates, Wollaston prisms, and fibers worsen the static minimal extinction ratio. This causes dephasing in case of atom transport and is transformed into noise by the locks even in the static case (see Table 2). Currently the biggest contribution to the static polarization impurity comes from the combining fiber.

Therefore I studied the fiber in more detail: I measured several PM fibers, none of which are significantly better than the 10^{-4} achieved by the built-in fiber. Then I tested a non-PM fiber, which had a minimal extinction ratio of 10^{-5}. To minimize the effects of temperature and pressure fluctuations on this fiber I built a stabilization box. Unfortunately the extinction ratio deteriorated to 10^{-4} before the stability measurement. Nonetheless an initial characterization of the box was possible. Although some issues with the temperature stability remain, it seems the stability of the fiber has been improved. Therefore I advise further investigation in this area.

Component	RMS
Wollaston Prism	10^{-6}
Waveplates	$< 10^{-6}$
Intensity Lock Loop	10^{-5}
Phase Lock Loop	10^{-5}
Fiber	10^{-4}

Table 2: Minimal Ext. Ratio per component

7 Acknowledgements

I greatly enjoyed the time of working on my bachelor thesis within the quantum technologies group and there are several people I would like to extend a special thank-you to.

First, I would like to thank professor Meschede for allowing me to write my bachelor thesis on the 1D Quantum Walk Experiment. My internship at this interesting and multifaceted experiment offered a great first introduction to the field of quantum optics. Both the experiment and the topic of my thesis became increasingly fascinating as I grasped more and more of the underlying physics. Although the limited time of a bachelor thesis allowed but a small glimpse into the experiment, it proved a great motivation to pursue a further career in research.

During my time in the group I had two main advisors, whom I am especially indebted to. I thank Dr. Andrea Alberti for his involvement in and support of my stay through extensive discussions and good suggestions. His level of overview over the experiment, and extensive knowledge of mathematical theorems are an inspiration for further studies. I thank Carsten Robens, my direct advisor, for allowing me to tag along - offering answers to questions and explanation of the key points of the experiment, as well as realistic feedback to ideas. I thank both Carsten and Andrea, as well as Martin Link for proofreading this thesis.

It was not only my advisors, but also the great atmosphere within the entire research group, that made for a great time. It was both a conducive working environment, as well as a very fun place to spend ones days: I felt very welcome and supported throughout my stay. At this point my special thanks go to Dr. Andreas Steffen and Ricardo Gomez Escalante for answering any number of impossible questions to the best of their knowledge, and with a good deal of enthusiasm. To Stefan Brakhane for his help with the stabilization measurements and control of the MBEDs. And to Dr. Wolfgang Alt for his phenomenal physics intuition, memory, as well as explanations and anecdotes of physical processes in any- and everything around us.

Last but not least I would like to acknowledge my family and friends, who condoned many random outbursts of physics, supported my endeavours, and kept me sane (to a certain extent) during the time of this thesis.

References

[1] Hahn, (1950), *Physical Review* Vol. 80, No. 4

[2] Richard P. Feynman, (1982), *International Journal of Theoretical Physics* Vol. 21, No. 6/7

[3] David W. Allan, (1987), *IEEE Transactions on ultrasonics, ferroelectrics, and frequency control*, Vol. UFFC-34 No 6

[4] Frederick M. Sears, (1990), *Journal of Lightwave Technology* Vol. 8 No. 5

[5] R. A. Cline, J. D. Miller, M. R. Matthews and D. J. Heinzen, (1994), *Opt. Lett. 19, 207*

[6] T. A. Savard, K. M. OHara, and J. E. Thomas, (1997), *Physical Review A* Vol 56, No 2

[7] Rudolf Grimm, Matthias Weidemüller, Yurii B. Ovchinnikov, (2000), *Advances in Atomic, Molecular and Optical Physics* Vol. 42, 95-170

[8] Schrader *et al.*, (2001), *Appl. Phys. B* 73, 819824

[9] Kuhr *et. al*, (2001), *Science* Vol 293

[10] Alt *et. al*, (2003), *Physical Review A* 67, 033403

[11] Kuhr *et. al*, (2005), *Physical Review A* 72, 023406

[12] Daniel A. Steck, (2010), *Cesium D Line Data*

[13] Steffen *et. al*, (2012), *PNAS* Vol. 109, No. 25

[14] Fam Le Kien, P. Schneeweiss, A Rauschenbeutel, (2013), *European Physics Journal* D 67:92; arXiv: 1211.2673v2

[15] PhD. thesis Stefan Kuhr, University of Bonn, (2003)

[16] PhD. thesis Wolfgang Alt, University of Bonn, (2004)

[17] Diplomthesis Daniel Döring, University of Bonn, (2007)

[18] PhD. thesis Michal Karski, University of Bonn, (2010)

[19] Master thesis Anna Hambitzer, University of Bonn, (2012)

[20] Datasheet for the FUD-3397 PM780-BK-S-BN Nufern fiber

[21] Thorlabs manual for the Manual Fiber Polarization Controller

[22] Thorlabs manual for connectorization and polishing of optical fibers

Figures 1, 2, 3, 4, 5, and 6 were taken from group-internal sources.